Article
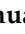
Zircon U-Pb-Hf Isotopes, Biotite ^{40}Ar/^{39}Ar Geochronology, and Whole-Rock Geochemistry of the Baogeqi Gabbro in the Northern Alxa, Southernmost Central Asian Orogenic Belt

Shaohua Zhang [1,*](ID), Chiyang Liu [2], Jianqiang Wang [2], Jianke Bai [3], Xiaochen Zhao [4], Long Zhang [1], Nan Jia [2,5], Lijun Song [1] and Heng Peng [2](ID)

[1] Shaanxi Key Laboratory of Petroleum Accumulation Geology, School of Earth Sciences and Engineering, Xi'an Shiyou University, Xi'an 710065, China; longzh1225@126.com (L.Z.); ljsong@xsyu.edu.cn (L.S.)
[2] State Key Laboratory of Continental Dynamics, Department of Geology, Northwest University, Xi'an 710065, China; lcy@nwu.edu.cn (C.L.); wjq@nwu.edu.cn (J.W.); jiananboy@126.com (N.J.); pengheng@stumail.nwu.edu.cn (H.P.)
[3] Research Center of Orogenic Geology, Xi'an Center of Geological Survey, China Geological Survey, Xi'an 710054, China; baijianke2003@163.com
[4] College of Geology and Environment, Xi'an University of Science and Technology, Xi'an 710054, China; zxc@xust.edu.cn
[5] Department of Geology, Liaoning Technical University, Fuxin 123000, China
[*] Correspondence: zhangshh@xsyu.edu.cn

Abstract: The final closure time of the Paleo-Asian Ocean and the Permo-Carboniferous tectonic settings in the northern Alxa are very important but controversial tectonic issues. The geochronology and petrogenesis of mafic igneous rocks are superior in clarifying regional tectonic settings. Here, we report on zircon U-Pb-Hf isotopes, biotite ^{40}Ar/^{39}Ar geochronology and whole-rock geochemical data of the hornblende gabbro from the Baogeqi gabbro pluton in the northern Alxa. The LA-ICP MS U-Pb analysis of zircon grains from the hornblende gabbro yield a weighted mean age of 262.7 ± 2.3 Ma (2σ, MSWD = 0.74), manifesting that the Baogeqi gabbro pluton emplacement was during the late Middle Permian (Capitanian). The ^{40}Ar/^{39}Ar dating of biotite grains from the hornblende gabbro yields a plateau age of 231.3 ± 1.6 Ma (2σ, MSWD = 0.55), indicating that the Baogeqi gabbro pluton cooled to below 300 °C in the Triassic. The hornblende gabbro samples are calc-alkaline with metaluminous character, and show enrichment in large ion lithophile elements (e.g., Rb, Ba, Sr, and K) but depletion in Nb, Ta, P, Th, and Ti relative to primitive mantle. Combined with the positive zircon εHf(t) values (+4.9–+9.4), we suggest that the magmas formed from the partial melting of depleted mantle were metasomatized by slab-derived fluids. Together with regional geology, these geochemical data suggest that the Baogeqi gabbro pluton was formed in an intracontinental extension setting, further indicating that the Paleo-Asian Ocean in the northern Alxa was closed prior to the late Middle Permian (Capitanian), and this region was in a post-collision extensional setting during the Capitanian-Late Permian. In addition, the Triassic cooling of the gabbro pluton may be a record of the decline of the Capitanian-Late Permian post-collisional extension basin due to the far-field effect of subduction-collision during the closure of the Paleo-Tethys Ocean.

Keywords: gabbro; geochronology; petrogenesis; the north Alxa; Paleo-Asian Ocean

1. Introduction

The Central Asian Orogenic Belt (CAOB) is composed of a large number of accretionary complexes, magmatic arcs, arc-related basins, ophiolites, seamounts, and continental fragments, which witnessed the long-term subduction and closure processes of the Paleo-Asian Ocean between the Siberia and East Europe cratons to the north, and the North China and Tarim cratons to the south (Figure 1a) [1–5]. Although a large number of works have been carried out on the CAOB, there is still no consensus on its geological evolution since

the Paleozoic, especially on the final closure time of the Paleo-Asian Ocean and the Permo-Carboniferous tectonic setting of the CAOB [4,6,7]. Previous studies on these issues mainly focused on the Junggar, Tianshan, Altai, and Beishan areas in the western segment of the CAOB, and the Xingmeng areas in the eastern segment of the CAOB [7–16], while the northern Alxa in the middle segment of the CAOB has received less attention [17–23].
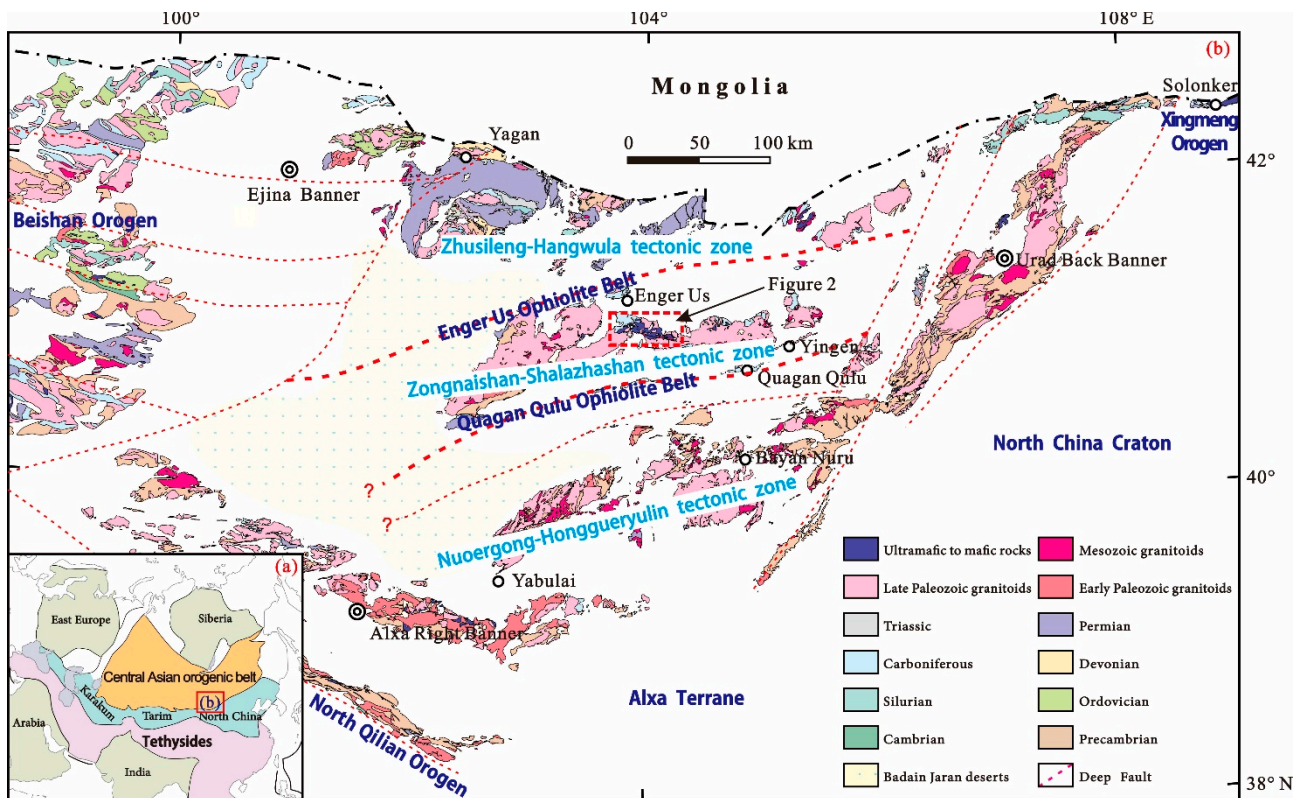

Figure 1. (**a**) Simplified tectonic sketch map of the Central Asian orogenic belt (CAOB) with the location of the studied area. Modified after [24]; (**b**) Geological map of the northern Alxa. Modified after [20].

Located at the junction between the North China Craton, Tarim Craton, and Mongolian microcontinents, the northern Alxa area is a part of the CAOB, and is therefore a key area for deciphering the evolution of the Paleo-Asian Ocean [18,23,25]. In terms of the closure time of the Paleo-Asian Ocean in the northern Alxa, there are currently three popular viewpoints: Devonian-Early Carboniferous [19,26]; late Early Permian-early Middle Permian [20,24,26], and latest Permian-Early Triassic [18,27]. Based on the closure time of the Paleo-Asian Ocean, three different perspectives are proposed regarding the Permo-Carboniferous tectonic setting: an intracontinental rift setting [19,25]; a tectonic transitional setting from subduction-collision to intracontinental extension [20,25,27], and a continuous subduction setting [18,28]. These disagreements suggest that more work is needed to clarify the closure time of the Paleo-Asian Ocean and the Permo-Carboniferous tectonic setting in the northern Alxa.

There is a consensus that mafic igneous rocks are superior in clarifying the tectonic settings of key periods due to their direct derivation from partial melting of the mantle [29–31]. Therefore, the Baogeqi gabbro pluton in the northern Alxa has become one of the best targets to constrain the closure time of the Paleo-Asian Ocean and the Permo-Carboniferous tectonic setting. In this contribution, we present new data on zircon U-Pb-Hf isotopes, biotite ^{40}Ar/^{39}Ar geochronology and whole-rock geochemistry of the hornblende gabbro from the Baogeqi gabbro pluton. Our results are used to provide new constraints on the petrogenesis, emplacement, and cooling of the Baogeqi gabbro pluton in the northern Alxa,

and shed light on the closure time of the Paleo-Asian Ocean and the Permo-Carboniferous tectonic setting.

2. Geological Background and Sample Description

The northern Alxa, situated in western Inner Mongolia of China, occupies the middle segment of the southernmost CAOB and connects the Xingmeng orogen to the east and the Beishan-Tianshan orogen to the west [4,32]. Regional geological works in the northern Alxa show that there are two ophiolite belts, i.e., Enger Us Ophiolite Belt in the north and Quagan Qulu Ophiolite Belt in the south [23]. In general, the Enger Us Ophiolite Belt is regarded as the final closure site of the Paleo-Asian Ocean, and the Quagan Qulu Ophiolite Belt is considered to be a suture related to the closure of a back-arc basin [17,23,33].

Based on the differences in stratigraphy, paleontology, and magmatism, these two ophiolite belts could divide the northern Alxa into three tectonic zones from north to south: the Zhusileng-Hangwula, the Zongnaishan-Shalazhashan, and Nuoergong-Honggueryulin tectonic zones (Figure 1b) [23]. The Zhusileng-Hangwula tectonic zone is composed mainly of Paleozoic-Mesozoic sedimentary rocks, with subordinate Late Paleozoic magmatic rocks and Precambrian rocks [17]. The Zongnaishan-Shalazhashan tectonic zone mainly consists of Late Paleozoic-Early Mesozoic magmatic rocks and Cretaceous sedimentary rocks, with subordinate Permo-Carboniferous sedimentary rocks, minor Early Paleozoic magmatic rocks, and Mesoproterozoic basement rocks [34,35]. The Nuoergong-Honggueryulin tectonic zone is characterized by widely outcropped Neoarchean-Paleoproterozoic basement rocks and Paleozoic-Mesozoic magmatic rocks [35,36].

The Baogeqi gabbro pluton is located in the middle part of the Zongnaishan-Shalazhashan tectonic zone. This pluton, covering an area of approximately 160 km^2 and extending in the EW direction for over 40 km, is the largest mafic intrusion in the Zongnaishan-Shalazhashan tectonic zone (Figure 2). The western part of the Baogeqi gabbro pluton was emplaced into the Upper Carboniferous to Lower Permian Amushan Formation (Figure 3a,b), while the east part of this pluton is in intrusive contact with later granitoid plutons. The hornblende gabbro samples are located at the western margin of the Baogeqi gabbro pluton. They have moderate-grained texture and are mainly composed of plagioclase and hornblende, with minor pyroxene and biotite (Figure 3c,d).
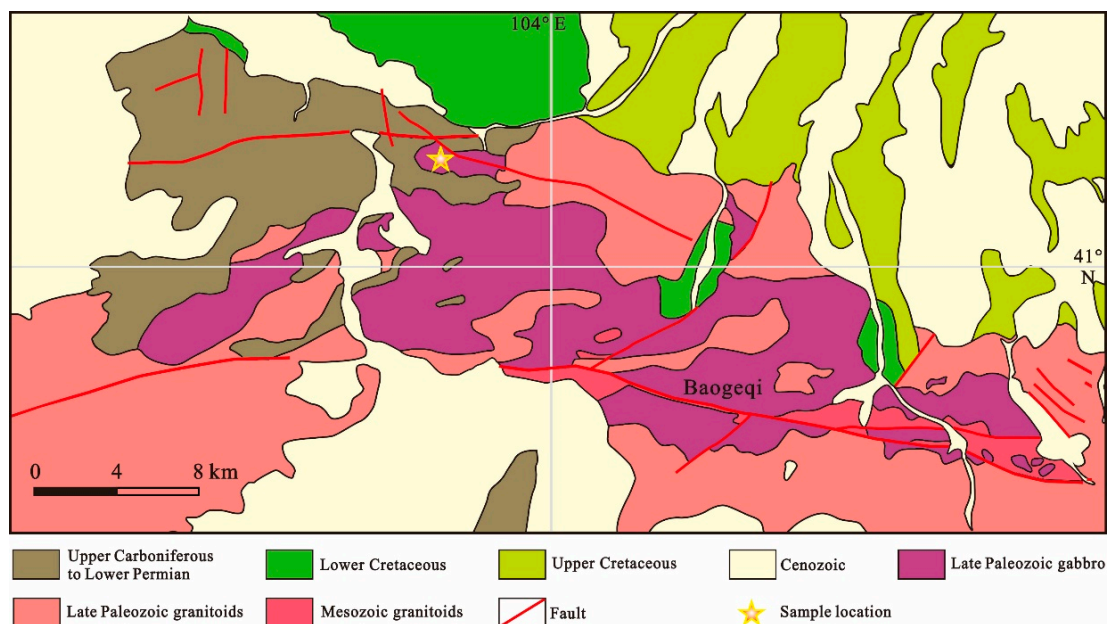

Figure 2. Geological map of the study area showing the distribution of the Baogeqi gabbro pluton.
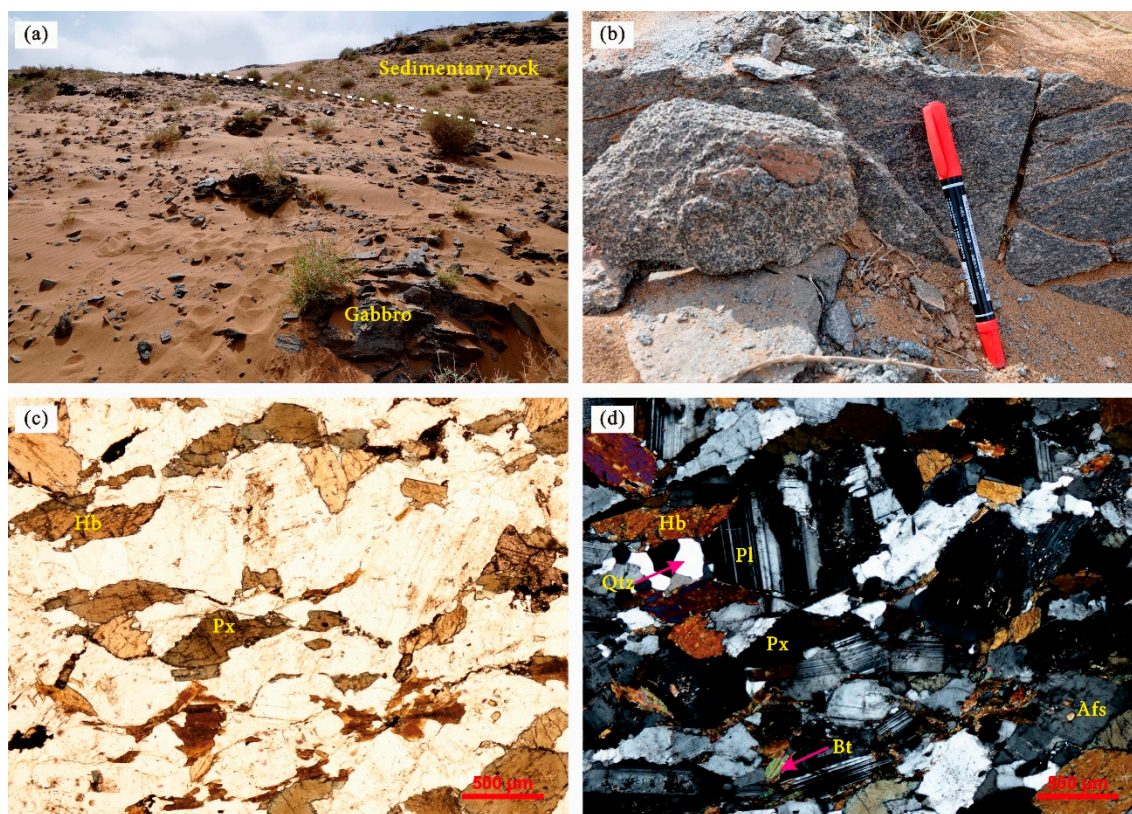
Figure 3. Field photographs and photomicrographs showing petrographic features of the hornblende gabbro from the Baogeqi gabbro plutonthe Baogeqi gabbro: (**a**) The intrusive contact relationship between the Baogeqi gabbro plutonthe Baogeqi gabbro and Amushan Formation sedimentary rocks; (**b**) Outcrop of the Baogeqi gabbro plutonthe Baogeqi gabbro; (**c**) The photomicrograph of the hornblende gabbrothe Baogeqi gabbro in plane polarized light, and (**d**) The photomicrograph of the hornblende gabbrothe Baogeqi gabbro under cross polarized light. Mineral abbreviations: Pl—plagioclase; Qtz—quartz; Hb—hornblende; Px—Pyroxene; Bt—biotite; Afs—Alkali feldspar.

3. Analytical Methods

In this study, the samples selected for zircon U-Pb-Hf isotopic, biotite ^{40}Ar/^{39}Ar geochronological, and whole-rock geochemical analyses were fresh and the least affected by post-magmatic weathering. Zircon grains and medium-sized (200–500 μm) biotite grains were separated using conventional heavy liquid and magnetic techniques in the Shangyi Geologic Service Co., Ltd., Langfang, Hebei Province, China. All analyses were performed at the State Key Laboratory of Continental Dynamics, Northwest University, Xi'an, China.

3.1. Zircon U-Pb Dating and Hf Isotope Analyses

About 150 zircon grains were randomly selected and mounted in epoxy resin and polished. Cathodoluminescence (CL) images were obtained using a Quanta 400FEG environmental scanning electron microscope equipped with an Oxford energy-dispersive spectroscopy system. In situ LA-ICP-MS zircon U-Pb dating was conducted on an Agilent 7500a ICP-MS instrument equipped with a 193 nm ArF excimer laser and a homogenizing imaging optical system. A fixed spot size of 32 μm with a laser repetition rate of 6 Hz was adopted throughout this study. Standard zircon 91500 and reference material GJ-1 were used for U-Pb isotopic ratio correction. The isotopic ratios were calculated using the GLITTER 4.0 program (Macquarie University, Ryde, Australia) and were corrected for both instrumental mass bias, depth-dependent elemental, and isotopic fractionation. Concordia diagrams and weighted mean calculations were made using the Isoplot program

(version 4.15) [37]. A detailed analytical procedure of age and trace element determinations of zircons can be found in [38].

In situ zircon Hf isotope analysis was undertaken on a Nu Plasma HR MC-ICP-MS (Nu Instrument Ltd., Wrexham, UK) equipped with a GeoLas 2005 193 nm ArF-excimer laser-ablation system. During analysis, a laser repetition rate of 10 Hz at 100 mJ was used and spot sizes were 44 μm. Helium was used as carrier gas. Zircon standards 91500 and Mud Tank were treated as quality control every ten unknown samples. The detailed analytical procedure was described by [39].

3.2. Biotite $^{40}Ar/^{39}Ar$ Dating

The concentrates of biotite were irradiated at the China Mianyang Research Reactor (CMRR) for 30 h with fluence monitors of ZBH-25 biotite (132.9 ± 1.3 Ma) [40]. The biotite $^{40}Ar/^{39}Ar$ dating was conducted on a multi-collector Argus VI noble gas mass spectrometer, linked to a UHV gas extraction/purification line and an ESI MIR10-30 10.6 CO_2 laser system. Mineral sample preparation and $^{40}Ar/^{39}Ar$ analytical methods were described in detail by [41]. The $^{40}Ar/^{39}Ar$ dating results were calculated and plotted using the ArArCALC software [42]. Decay constant used were those given by [43]. Correction factors for interfering isotopes were calculated from analyses of co-irradiated Ca-glass samples and K-glass samples, and are $(^{40}Ar/^{39}Ar)_K = 0.00232$, $(^{39}Ar/^{37}Ar)_{Ca} = 0.000617$, and $(^{36}Ar/^{37}Ar)_{Ca} = 0.000235$.

3.3. Whole-Rock Geochemical Analyses

For geochemical analysis, fresh whole-rock samples were crushed in an agate mill to ~200 mesh. Major element contents were determined using a Rikagu RIX 2100 X-ray fluorescence (XRF) spectrometer, with analytical uncertainties lower than 5%. Trace element concentrations were analyzed by using an Agilent 7700a inductively coupled plasma mass spectrometer (ICP-MS), employing United States Geological Survey (USGS) and international rock standards (BHVO-2, AGV-2, BCR-2, and GSP-1). The analytical precision and accuracy for most of the trace elements were better than 5% [38].

4. Results

4.1. Zircon U-Pb Ages and Hf Isotope Compositions

Zircon U-Pb dating results are presented in Table A1 and Figure 4. Zircon grains of the hornblende gabbro from the Baogeqi gabbro pluton are mostly subhedral-euhedral prismatic crystals, ranging in size from 140 to 300 μm with aspect ratios between 1:1 and 3:1. In CL images, they commonly exhibited fine-scale and striped absorption oscillatory zoning (Figure 4a). Zircon trace element compositions revealed that they have variable Th and U contents of 13–2644 ppm and 58–2688 ppm, respectively, corresponding to Th/U ratios of 0.10–1.49, indicative of a magmatic origin. Twenty-five grains were selected for zircon U-Pb dating using LA-ICP-MS. Two of the analytical spots had a discordance > 10% and were rejected. The other 23 analytical spots were concordant and yielded a weighted mean $^{206}Pb/^{238}U$ age of 262.7 ± 2.3 Ma (2σ, MSWD = 0.74) (Figure 4a,b).

Fifteen grains that were previously analyzed by U–Pb methods were also analyzed for Lu–Hf isotopes on the same spot, and the results are presented in Table A2 and Figure 4. Fifteen analyses displayed $^{176}Lu/^{177}Hf$ and $^{176}Hf/^{177}Hf$ ratios of 0.000212–0.007454 and 0.282762–0.282880, respectively. Their age-corrected εHf(t) values ranged from +4.9 to +9.4 (Figure 4c), corresponding to single-stage zircon Hf model ages (T_{DM1}) of 794–529 Ma (Figure 4d), and two-stage zircon Hf model ages (T_{DM2}) of 991–689 Ma.
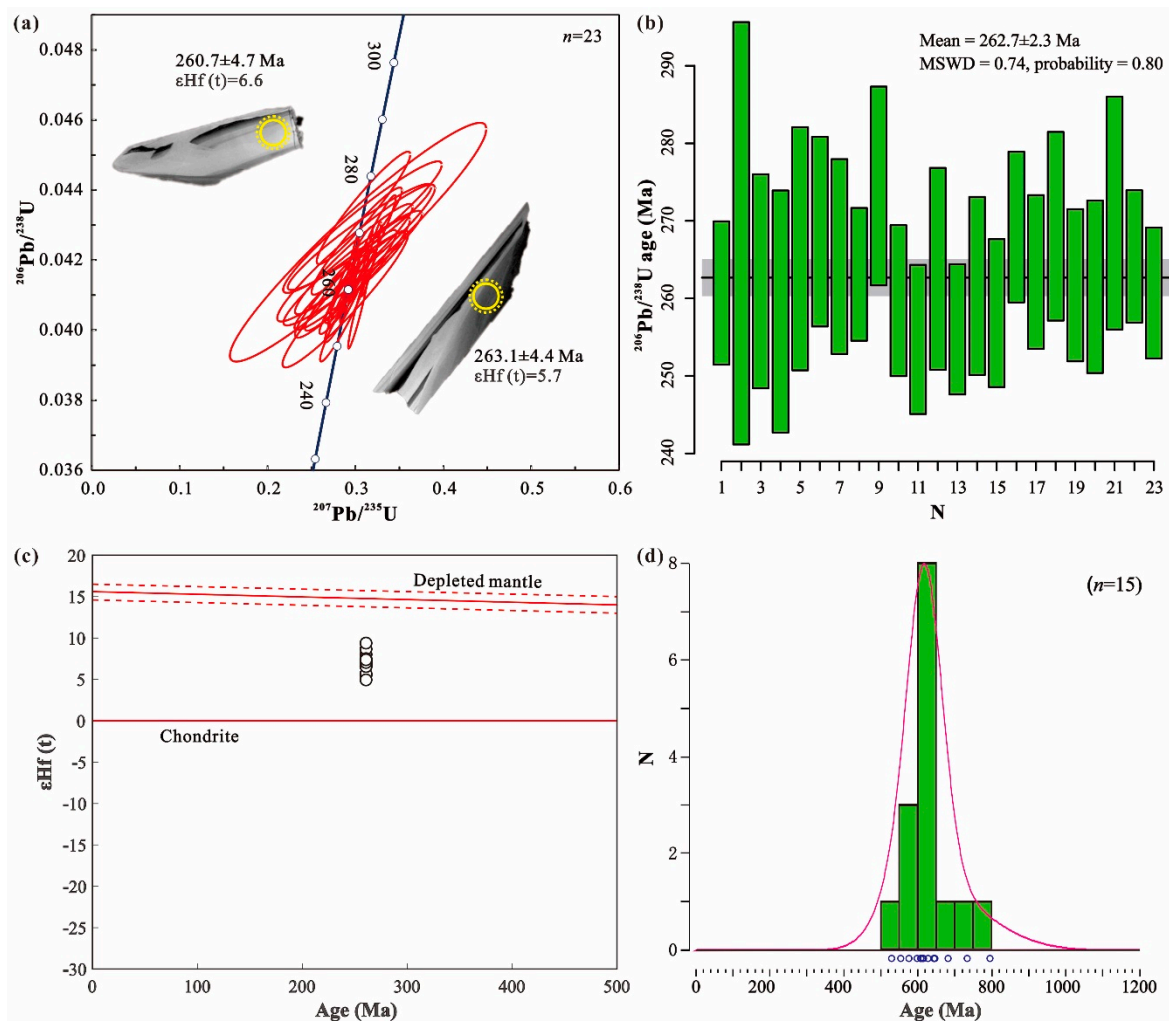
Figure 4. The diagrams for zircon U-Pb-Hf isotopes of the hornblende gabbro from the Baogeqi gabbro pluton: (**a**) Representative zircon cathodoluminescence images and U-Pb concordia diagram; (**b**) Weight mean plot of the concordant ages; (**c**) Plot of zircon εHf(t) values vs. U-Pb ages; (**d**) Histograms of T_{DM1} model ages of zircons.

4.2. Biotite $^{40}Ar/^{39}Ar$ Geochronology

The biotite $^{40}Ar/^{39}Ar$ stepwise heating results for the hornblende gabbro from the Baogeqi gabbro pluton are given in Table A3 and Figure 5. Nineteen laser heating stages were carried out for the sample, and stages 8–18 yielded a wide flat age spectrum with plateau age of 231.6 ± 1.6 Ma (2σ), corresponding to 65.14% of the total ^{39}Ar released and MSWD = 0.55 (Figure 5a). On the inverse $^{40}Ar/^{39}Ar$ isochron diagram, the data points defined an isochron with an age of 230.8 ± 6.9 Ma (2σ), corresponding to an initial $^{40}Ar/^{36}Ar$ ratio of 300 ± 70 and MSWD = 0.61 (Figure 5b).
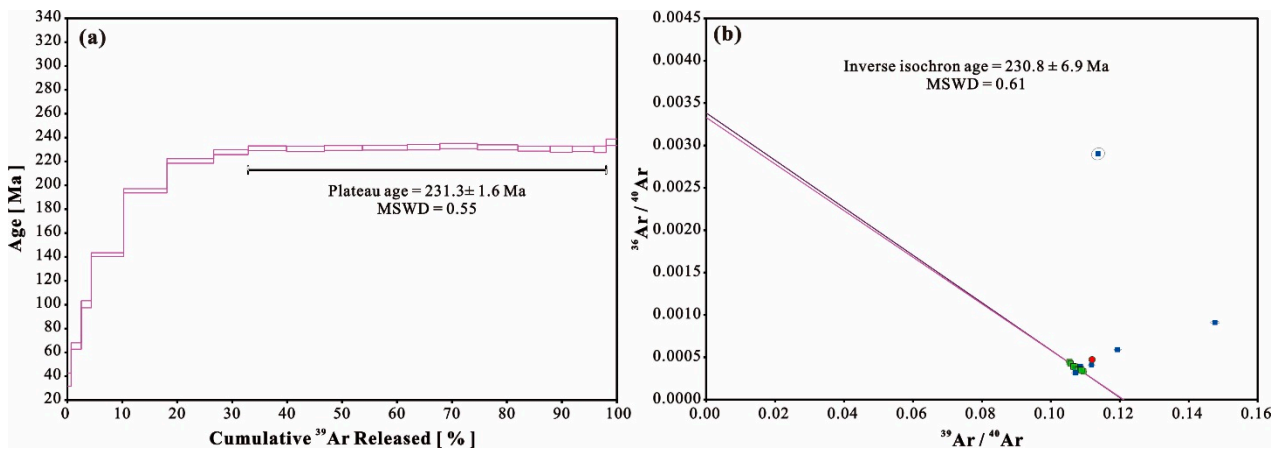
Figure 5. (**a**) Apparent age spectra and (**b**) inverse isochron diagram for biotite from the hornblende gabbro of the Baogeqi gabbro pluton obtained from $^{40}Ar/^{39}Ar$ step heating analyses.

4.3. Whole-Rock Geochemistry

The analytical results of whole-rock major and trace element compositions are listed in Table A4. The studied four hornblende gabbro samples showed SiO_2 = 51.90~54.99 wt. %, TiO_2 = 1.37~1.46 wt. %, Al_2O_3 = 18.41~20.11 wt. %, total Fe_2O_3 = 7.24~7.63 wt. %, MgO = 3.48~3.77 wt. %, CaO = 7.40~8.21 wt. %, Na_2O = 3.90~4.45 wt. %, K_2O = 1.18~1.24 wt. %, P_2O_5 = 0.19~0.22 wt. %, and Mg# values of 52.32~53.63. The total alkali-silica (TAS) diagram displays the majority of the rocks as gabbro with geochemical traits of calc-alkaline and metaluminous character (Figure 6).
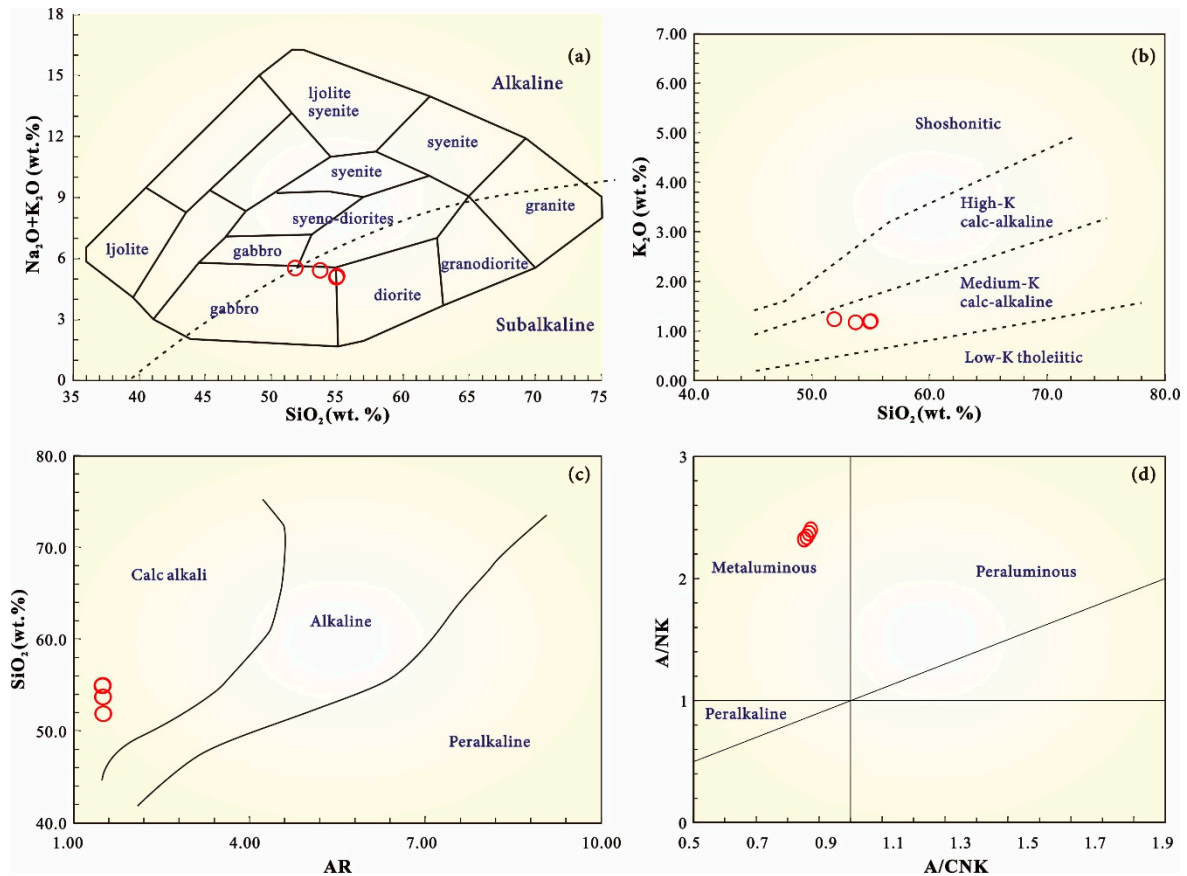
Figure 6. Geochemical diagrams for the hornblende gabbro samples from the Baogeqi gabbro pluton: (**a**) $Na_2O + K_2O$ vs. SiO_2 [44]; (**b**) K_2O vs. SiO_2 [45]; (**c**) A.R vs. SiO_2 [46], and (**d**) A/CNK vs. A/NK [47].

The studied hornblende gabbro samples have low concentrations of Cr (7.47~17.20 ppm) and Ni (6.87~7.25 ppm). In the chondrite-normalized REE diagram (Figure 7a), they display a slight enrichment of light rare earth element (LREE) ($[La:Yb]_N$ = 3.52~4.80) and minor negative Eu anomalies (δEu = 0.90~0.91). On the primitive mantle-normalized spider diagram (Figure 7b), all samples are enriched in large ion lithophile elements (LILEs, such as Rb, Ba, Sr, and K) and depleted in high field strength elements (HFSEs, i.e., Nb, Ta, P, Th, and Ti).

Figure 7. (**a**) Chondrite-normalized REE patterns and (**b**) primitive mantle-normalized trace element patterns for the hornblende gabbro samples from the Baogeqi gabbro pluton. The normalization values of chondrite are from [48] and data for primitive mantle are from [49].
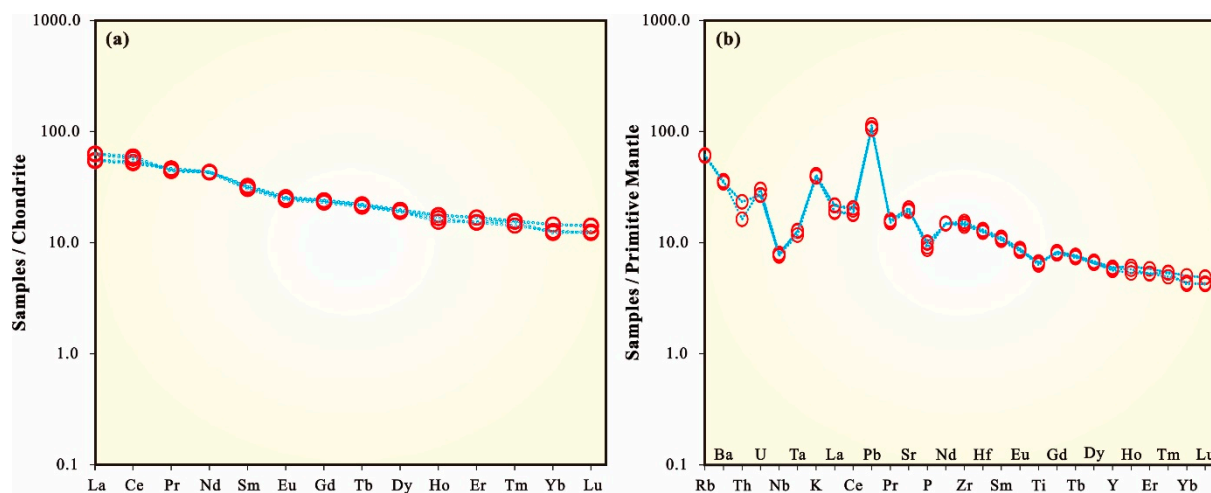
5. Discussions

5.1. Interpretation of the Zircon U-Pb and Biotite $^{40}Ar/^{39}Ar$ Ages

The LA-ICP-MS U-Pb isotope analyses on zircon grains from the hornblende gabbro sample yielded a weighted mean $^{206}Pb/^{238}U$ age of 262.7 ± 2.3 Ma (2σ, MSWD = 0.74), which was identical to the ages of 264 ± 3 Ma and 262 ± 4 Ma previously obtained from the Baogeqi gabbro pluton [34,50]. The CL morphology and internal structures, combined with high Th/U ratios (0.10–1.49) of the zircon grains, were indicative of their magmatic origin. Thus, the 262.7 ± 2.3 Ma (2σ) was interpreted as the crystallization age of these zircon grains, suggesting that the Baogeqi gabbro was emplaced in the late Middle Permian (Capitanian).

In this study, the $^{40}Ar/^{39}Ar$ dating of biotite grains from the gabbro sample yielded a plateau age of 231.3 ± 1.6 Ma (2σ). The low MSWD values (0.55) and 65.14% of the total ^{39}Ar released of the studied sample suggest that this age is reliable. It is worth noting that this $^{40}Ar/^{39}Ar$ age was younger than the 262.7 ± 2.3 Ma (2σ) U-Pb zircon crystallization age from the same sample. Previous studies have shown that the closure temperature of biotite in the Ar-Ar system was roughly ~300 °C [51]. Due to the lack of significant superimposed late deformation for the Baogeqi gabbro pluton, this biotite $^{40}Ar/^{39}Ar$ age can be interpreted to represent the time of cooling below ~300 °C.

5.2. Magma Source and Petrogenesis

The samples in this study are basaltic rocks with low SiO_2 contents, which suggested that their primary magmas were originated from the mantle. Zircons from the hornblende gabbro sample of the Baogeqi gabbro pluton have positive εHf(t) values from +4.9 to +9.4 and displayed an evolutionary trend between the depleted mantle and chondrite (Figure 4c), suggesting that the primary magmas were possibly originated from a relatively depleted mantle source [52,53]. However, in the chondrite-normalized REE diagrams and primitive mantle-normalized trace-element diagrams (Figure 7), the samples show LILE enrichment (e.g., Rb, Ba, Sr, and K) and HFSE depletion (e.g., Nb, Ta, P, Th, and Ti), which

are significantly different from depleted mantle-derived magmas. These characteristics indicate that the source of the magma was an enriched mantle or a depleted mantle influenced by crustal contamination. In addition, the samples have single-stage zircon Hf model ages (794–529 Ma) older than their crystallization ages (262.7 ± 2.3 Ma, 2σ), which also indicated that the source of the magma was enriched mantle or was influenced by crustal contamination [53].

It is generally accepted that crustal materials are rich in Zr and Hf, but depleted in Nb and Ta. Therefore, extensive crustal contamination might produce significant negative Nb and Ta anomalies, accompanied by positive Zr and Hf anomalies [54]. The studied hornblende gabbro samples were characterized by slight negative Nb and Ta anomalies and no obvious Zr and Hf anomalies, which probably implied negligible crustal contamination. Moreover, mantle-derived magmas unusually had low Lu/Yb ratios (0.14~0.15), while continental crust had relatively high Lu/Yb ratios (0.16~0.18) [49]. The studied hornblende gabbro samples had Lu/Yb ratios in the range of 0.14~0.15, which also suggested insignificant crustal contamination. In addition, the positive in situ zircon εHf (t) values (+4.9–+9.4) and absence of xenolith of these hornblende gabbro samples further ruled out the possibility of notable crustal contamination.

Generally, the fluids derived from dehydration of the altered oceanic crust or subducted sediment and melts of the oceanic slab or subducted sediment are usually enriched in LILEs and depleted in HFSEs [55]. Thus, the geochemical features of the studied hornblende gabbro samples suggested that the parent magma was modified by subduction-related fluids or melts. In the La/Nb vs. La/Ba diagram (Figure 8a), the studied hornblende gabbro samples show low La/Ba ratios with high La/Nb values, which indicated a tendency for subduction-modified lithospheric mantle. Furthermore, the studied samples plot near E-MORE but deviate from the MORB-OIB evolution line in the Nb/Yb vs. Th/Yb diagram (Figure 8b), which also suggested the influence of subduction components. Trace element ratios can be used to differentiate between fluid or melt-related enrichments during subduction [56]. In the Nb/Zr vs. Th/Zr and Nb/Zr vs. Ce/Y diagrams (Figure 8c,d), the studied samples show a tendency for fluid-related enrichment, which indicated that the magma source was likely modified by subduction-related fluids.

The hornblende gabbro samples of the Baogeqi gabbro pluton had lower Mg#, Cr, and Ni contents than the primary magma of basaltic melts (Mg# > 73; Cr > 1000 ppm, and Ni > 400 ppm), which probably indicated fractionation of olivine and pyroxene during the magma evolution [57]. In addition, the studied samples showed no obvious negative anomaly of Eu and Sr, which implied insignificant plagioclase fractionation.

Collectively, the hornblende gabbro of the Baogeqi gabbro pluton may be derived from the partial melting of depleted mantle metasomatized by slab-derived fluids, and subsequently experienced significant fractionation of olivine and pyroxene, but insignificant crustal contamination during magma evolution.
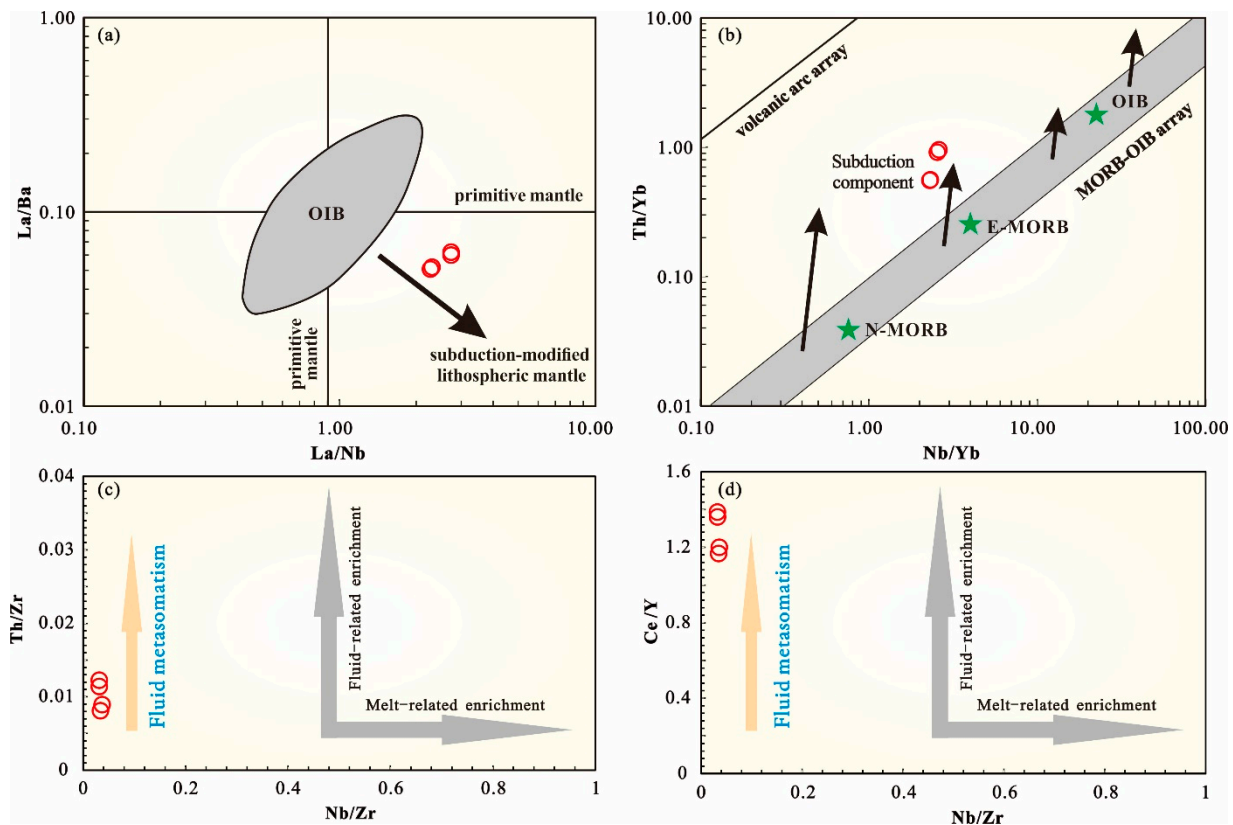
Figure 8. Binary plots of the hornblende gabbro samples from the Baogeqi gabbro pluton: (**a**) La/Ba vs. La/Nb [58]; (**b**) Th/Yb vs. Nb/Yb [59]; (**c**) Nb/Zr vs. Th/Zr [60]; (**d**) Nb/Zr vs. Ce/Y [56].

5.3. Tectonic Implications

The Permo-Carboniferous tectonic setting in the northern Alxa has been debated with various models including an intracontinental rift setting, a subduction setting or a tectonic transitional setting from subduction-collision to intracontinental extension [18–21]. Although our data from the hornblende gabbro samples of the Baogeqi gabbro pluton had some subduction imprints, they showed relatively high TiO_2 and Nb content, which was markedly different from those of volcanic arc mafic rocks in subduction settings [61]. In the Zr vs. Zr/Y and Nb×2-Zr/4-Y diagrams (Figure 9), the studied samples all fall in the field of within-plate setting, which implied a continental rift setting for the Baogeqi gabbro. In addition, the Baogeqi gabbro and synchronous extensive granites together formed a bimodal plutonic suite in the northern Alxa [34], which also supported an extensional setting during the late Middle Permian times. This interpretation is also supported by the regional geology. Magmatism, sedimentology, and provenance studies showed that the Paleo-Asian Ocean in the northern Alxa had been closed at the end of the Early Permian, and the late Middle Permian had entered a post-collisional extension stage [20,25,27,34]. Therefore, the Paleo-Asian Ocean in the northern Alxa was closed prior to the late Middle Permian (Capitanian), and this region stepped into a post-collisional extension basin evolutionary stage during the Capitanian-Late Permian.
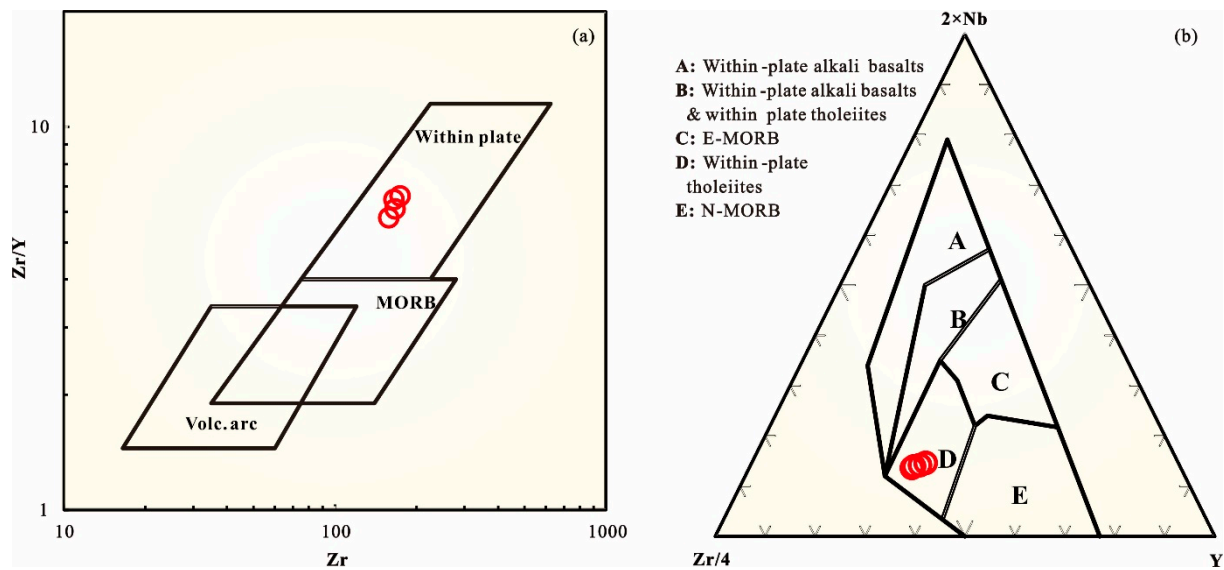
Figure 9. Tectonic environment discrimination diagrams for the hornblende gabbro samples of the Baogeqi gabbro pluton: (**a**) Zr/Y vs. Zr [62] and (**b**) Nb×2−Zr/4−Y [63].

The biotite ^{40}Ar/^{39}Ar age of the hornblende gabbro from the Baogeqi gabbro pluton with 231.3 ± 1.6 Ma (2σ) suggested that there was a cooling and exhumation event in the northern Alxa during Triassic times. In fact, the Triassic cooling and exhumation event was also documented in the adjacent area of the Baogeqi gabbro based on ^{40}Ar/^{39}Ar dating, apatite U-Pb, and fission track thermochronology [64,65]. The stratigraphic contact relationship of the northern Alxa also suggested that this region experienced a cooling and exhumation event during the Triassic times, characterized by high-angle unconformity between the strongly deformed Paleozoic strata and gently deformed Mesozoic strata. From the viewpoint of regional tectonics, the Paleo-Tethys Ocean in the southern North China-Tarim craton was closed during the Triassic [32,66–70]. Therefore, the Triassic cooling and exhumation event in the northern Alxa may be a record of the decline of the Capitanian-Late Permian post-collisional extension basin due to the far-field effect of subduction-collision during the closure of the Paleo-Tethys Ocean.

6. Conclusions

(1) The hornblende gabbro from the Baogeqi gabbro pluton in the northern Alxa yielded a LA-ICP MS zircon U-Pb age of 262.7 ± 2.3 Ma (2σ), manifesting that the Baogeqi gabbro pluton shaping was during the late Middle Permian (Capitanian). The ^{40}Ar/^{39}Ar dating of biotite grains from the Baogeqi gabbro pluton yielded a plateau age of 231.3 ± 1.6 Ma (2σ), which suggested that the pluton cooled to below 300 °C in the Triassic.

(2) The Baogeqi gabbro pluton formed as a result of the partial melting of depleted mantle metasomatized by slab-derived fluids, and subsequently experienced significant fractionation of olivine and pyroxene, but insignificant crustal contamination during magma evolution.

(3) The Baogeqi gabbro pluton intruded in an intracontinental extension setting, which implied that the Paleo-Asian Ocean in the northern Alxa was closed prior to the late Middle Permian (Capitanian), and this region stepped into a post-collisional extension basin evolutionary stage during the Capitanian-Late Permian. The Triassic cooling of the gabbro pluton may be a record of the decline of the Capitanian-Late Permian post-collisional extension basin due to the far-field effect of subduction-collision during the closure of the Paleo-Tethys Ocean.

Author Contributions: Conceptualization, S.Z.; Data curation, J.W. and J.B.; Formal analysis, J.B.; Funding acquisition, S.Z., C.L. and J.W.; Investigation, J.W., J.B., X.Z., L.Z., N.J., L.S. and H.P.; Methodology, J.B., L.S. and H.P.; Project administration, C.L. and J.W.; Resources, X.Z. and N.J.;

Software, X.Z. and L.Z.; Supervision, C.L.; Visualization, L.Z., N.J. and L.S.; Writing—original draft, S.Z.; Writing—review and editing, S.Z. All authors have read and agreed to the published version of the manuscript.

Data Availability Statement: Data are contained within the Appendix A.

Conflicts of Interest: The authors declare no conflict of interest.

Appendix A

Table A1. LA-ICP-MS U-Pb isotope analytical results for zircon crystals from the hornblende gabbro of the Baogeqi gabbro pluton.

| Analysis_# | Isotope Ratios | | | | | | | | Ages | | | | | | | | Best Ages | 1 s |
	Pb^{207}/Pb^{206}	1 s	Pb^{207}/U^{235}	1 s	Pb^{206}/U^{238}	1 s	Pb^{208}/Th^{232}	1 s	Pb^{207}/Pb^{206}	1 s	Pb^{207}/U^{235}	1 s	Pb^{206}/U^{238}	1 s	Pb^{208}/Th^{232}	1 s		
171025C112	0.05134	0.00277	0.29203	0.01532	0.04127	0.00076	0.01321	0.00033	256.2	119.41	260.2	12.04	260.7	4.72	265.3	6.63	260.7	4.72
171025C113	0.05173	0.01663	0.3031	0.09637	0.04251	0.00225	0.0132	0.00339	273.7	605.87	268.8	75.09	268.4	13.9	265.1	67.7	268.4	13.9
171025C114	0.05186	0.00764	0.2967	0.0432	0.04151	0.00114	0.01364	0.00113	279.1	306.25	263.8	33.83	262.2	7.05	273.9	22.44	262.2	7.05
171025C115	0.05121	0.0085	0.28864	0.04729	0.04089	0.00129	0.01225	0.00214	250.5	343.03	257.5	37.27	258.3	7.97	246.1	42.76	258.3	7.97
171025C116	0.05173	0.01029	0.30086	0.05934	0.0422	0.00129	0.01729	0.00182	273.4	401.3	267.1	46.32	266.4	8	346.5	36.15	266.4	8
171025C118	0.05143	0.00588	0.3016	0.03401	0.04254	0.00101	0.01393	0.00074	260.2	242.84	267.6	26.53	268.6	6.24	279.6	14.85	268.6	6.24
171025C119	0.05148	0.00771	0.29825	0.04425	0.04203	0.00104	0.01533	0.00145	262.2	311.61	265	34.61	265.4	6.41	307.4	28.95	265.4	6.41
171025C120	0.05127	0.00122	0.29437	0.0062	0.04165	0.00071	0.01255	0.0002	252.8	53.94	262	4.86	263.1	4.37	252.1	3.96	263.1	4.37
171025C121	0.05157	0.00595	0.30921	0.03518	0.04349	0.00106	0.01444	0.00089	266.3	244.89	273.6	27.29	274.5	6.54	289.7	17.66	274.5	6.54
171025C122	0.05151	0.00389	0.2919	0.02165	0.0411	0.0008	0.01389	0.00075	263.8	164.5	260.1	17.02	259.7	4.97	278.9	15.04	259.7	4.97
171025C126	0.05137	0.00315	0.28546	0.01698	0.0403	0.00079	0.01308	0.00038	257.4	134.95	255	13.41	254.7	4.91	262.7	7.62	254.7	4.91
171025C127	0.05157	0.00911	0.29698	0.05209	0.04177	0.0008	0.01413	0.00163	266.2	361.62	264	40.78	263.8	6.65	283.7	32.48	263.8	6.65
171025C128	0.0542	0.00146	0.30282	0.00731	0.04052	0.00069	0.01212	0.0002	379.3	59.14	268.6	5.7	256	4.29	243.4	3.98	256	4.29
171025C129	0.0516	0.00609	0.29468	0.03437	0.04142	0.00095	0.01367	0.00085	267.7	250.08	262.2	26.96	261.6	5.86	274.4	16.91	261.6	5.86
171025C132	0.05152	0.00301	0.29021	0.01644	0.04085	0.00079	0.01305	0.00037	264.3	128.85	258.7	12.94	258.1	4.87	262.1	7.35	258.1	4.87
171025C133	0.05479	0.00278	0.32219	0.01571	0.04264	0.0008	0.01329	0.00035	403.7	109.33	283.6	12.06	269.2	4.96	266.9	6.93	269.2	4.96
171025C134	0.0514	0.00287	0.29565	0.01589	0.04171	0.00082	0.01378	0.00036	258.7	123.14	263	12.45	263.4	5.06	276.6	7.12	263.4	5.06
171025C135	0.05181	0.00924	0.30479	0.05405	0.04266	0.001	0.01421	0.00072	276.9	364.03	270.1	42.06	269.3	6.21	285.2	14.28	269.3	6.21
171025C136	0.05184	0.00361	0.29618	0.02016	0.04143	0.00081	0.01204	0.00066	278.6	151.86	263.4	15.8	261.7	5.01	241.8	13.26	261.7	5.01
171025C140	0.0518	0.00737	0.29389	0.04173	0.0414	0.00092	0.01484	0.00103	262.3	299.13	261.6	32.75	261.5	5.68	297.7	20.47	261.5	5.68
171025C142	0.05202	0.01015	0.30809	0.05965	0.04294	0.00124	0.014	0.00186	286.4	393.74	272.7	46.3	271	7.66	281.1	37.1	271	7.66
171025C143	0.05486	0.00143	0.31799	0.00739	0.04203	0.0007	0.01262	0.0002	406.5	56.76	280.4	5.69	265.4	4.36	253.6	3.95	265.4	4.36
171025C144	0.05169	0.00148	0.29414	0.00763	0.04126	0.0007	0.01264	0.0002	271.7	64.35	261.8	5.99	260.7	4.31	253.8	4.06	260.7	4.31

Table A2. Zircon LA-MC-ICP-MS Lu-Hf isotope analytical results for the hornblende gabbro of the Baogeqi gabbro pluton.

Analysis_#	Hf176/Hf177corr′	1σ	′Yb176/Hf177′	1σ	′Lu176/Hf177′	1σ	εHf(0)	εHf(t)	TDM1 (Ma)	TDM2 (Ma)	fLu/Hf	Age (Ma)
10540	0.282801	0.000017	0.04	0.00	0.001193	0.000016	1.0	6.6	642.6	870.6	−1.0	260.7
10541	0.282762	0.000019	0.01	0.00	0.000254	0.000002	−0.4	5.5	681.7	942.8	−1.0	268.4
10542	0.282806	0.000013	0.02	0.00	0.000636	0.000003	1.2	6.8	627.3	852.8	−1.0	262.2
10543	0.282816	0.000013	0.01	0.00	0.000355	0.000010	1.6	7.2	607.8	827.2	−1.0	258.3
10544	0.282799	0.000016	0.04	0.00	0.001052	0.000017	1.0	6.6	643.6	870.7	−1.0	266.4
10545	0.282819	0.000016	0.04	0.00	0.001027	0.000012	1.7	7.4	615.1	824.1	−1.0	268.6
10546	0.282817	0.000015	0.01	0.00	0.000405	0.000004	1.6	7.4	607.6	821.8	−1.0	265.4
10547	0.282796	0.000026	0.20	0.00	0.005410	0.000055	0.8	5.7	733.2	940.6	−0.9	263.1
10548	0.282788	0.000015	0.01	0.00	0.000212	0.000002	0.6	6.5	645.2	879.9	−1.0	274.5
10549	0.282839	0.000011	0.01	0.00	0.000292	0.000002	2.4	8.0	575.6	774.7	−1.0	259.7
10550	0.282816	0.000015	0.02	0.00	0.000588	0.000017	1.5	7.0	612.2	833.6	−1.0	254.7
10551	0.282854	0.000017	0.01	0.00	0.000214	0.000001	2.9	8.7	553.1	736.2	−1.0	263.8
10552	0.282788	0.000026	0.27	0.00	0.007454	0.000024	0.6	4.9	793.9	990.6	−0.8	256
10553	0.282880	0.000022	0.03	0.00	0.001063	0.000041	3.8	9.4	528.7	689.5	−1.0	261.6
10554	0.282827	0.000016	0.02	0.00	0.000677	0.000021	1.9	7.5	597.8	807.0	−1.0	258.1

Table A3. Results of ^{40}Ar/^{39}Ar laser stepwise heating analysis of biotite for the hornblende gabbro of the Baogeqi gabbro pluton.

Step	Laser Output	36Ar (fA)	%1 s	37Ar (fA)	%1 s	38Ar (fA)	%1 s	39Ar (fA)	%1 s	40Ar (fA)	%1 s	40(r)/39(k)	±2 s	Age (Ma)	±2 s	40Ar(r) (%)	39Ar(k) (%)	K/Ca	±2 s
1	1.6%	0.2254237	1.162	0.401899	464.185	0.178399	36.388	8.8307	0.772	77.688	0.341	1.25504	±0.18861	37.04	±5.51	14.27	0.70	9.4	±87.7
2	1.7%	0.2818844	1.197	1.057066	170.176	0.346796	16.205	23.1992	0.258	134.839	0.197	2.23204	±0.09267	65.36	±2.67	38.24	1.84	9.4	±32.1
3	1.8%	0.1786040	2.058	3.921543	52.938	0.286580	17.141	22.7355	0.272	130.905	0.199	3.46101	±0.10548	100.37	±2.98	59.85	1.80	2.5	±2.6
4	1.9%	0.4586787	0.882	4.854332	38.710	0.892186	5.784	74.4875	0.103	502.664	0.056	4.95199	±0.05474	141.94	±1.51	73.07	5.91	6.6	±5.1
5	2.0%	0.4889235	0.821	4.890746	43.155	1.119572	4.619	99.1750	0.098	827.718	0.034	6.91981	±0.06545	195.40	±1.75	82.56	7.87	8.7	±7.5
6	2.1%	0.3915543	0.860	2.196581	88.223	1.151732	4.468	107.2098	0.086	955.144	0.029	7.86231	±0.07111	220.45	±1.88	87.88	8.51	21.0	±37.0
7	2.2%	0.2837264	1.451	0.056881	3508.245	0.865273	5.813	78.9673	0.096	724.268	0.039	8.14217	±0.07802	227.82	±2.05	88.40	6.27	597.0	±41,886.2
8	2.3%	0.3213924	0.960	2.218927	87.059	0.905501	5.558	87.9912	0.106	819.334	0.036	8.26671	±0.07592	231.09	±1.99	88.40	6.98	17.1	±29.7
9	2.4%	0.3640906	1.321	1.830119	128.671	1.027297	5.005	86.6589	0.106	819.044	0.170	8.24393	±0.08598	230.49	±2.26	86.86	6.88	20.4	±52.4
10	2.5%	0.3494436	1.296	0.594308	277.081	0.962951	5.627	87.4059	0.103	823.641	0.036	8.27494	±0.07919	231.31	±2.08	87.44	6.94	63.2	±350.5
11	2.6%	0.3817004	0.794	1.848284	89.057	1.090187	4.223	102.5864	0.100	959.064	0.032	8.28339	±0.07490	231.53	±1.97	88.23	8.14	23.9	±42.5
12	2.7%	0.2730679	1.426	1.702447	86.659	0.750930	7.958	74.8276	0.101	699.268	0.199	8.30115	±0.08749	231.99	±2.29	88.45	5.94	18.9	±32.8
13	2.8%	0.2886769	1.305	1.851081	100.068	0.939169	5.819	86.4050	0.093	802.872	0.173	8.33923	±0.08380	232.99	±2.20	89.37	6.86	20.1	±40.2
14	3.0%	0.3039803	1.147	1.717501	91.993	0.934860	5.549	92.2932	0.086	852.278	0.165	8.29532	±0.08158	231.84	±2.14	89.45	7.33	23.1	±42.5
15	3.1%	0.2383410	1.750	2.097129	87.780	0.816090	6.968	74.2499	0.103	680.806	0.040	8.25525	±0.08016	230.79	±2.10	89.65	5.89	15.2	±26.7
16	3.3%	0.1647683	2.506	0.325949	476.262	0.473234	9.758	50.7882	0.298	465.429	0.058	8.23843	±0.09901	230.35	±2.60	89.52	4.03	67.0	±638.2
17	3.5%	0.1497405	2.104	0.431213	419.214	0.465162	12.081	49.6386	0.145	451.852	0.061	8.24461	±0.08417	230.51	±2.21	90.19	3.94	49.5	±415.0
18	3.7%	0.0897321	3.339	2.319148	86.503	0.293219	20.549	27.8715	0.232	254.932	0.104	8.23400	±0.10453	230.23	±2.74	89.64	2.21	5.2	±8.9
19	3.9%	0.0725327	3.323	2.029225	87.103	0.230824	22.407	24.5160	0.238	227.873	0.122	8.46020	±0.10418	236.16	±2.73	90.63	1.95	5.2	±9.0

J = 0.01649000 ± 0.00005442.

Table A4. Major (wt. %) and trace element compositions (in ppm) for the hornblende gabbro of the Baogeqi gabbro pluton.

Sample	YE17-65A	YE17-65B	YE17-65	YE17-65C
SiO_2	54.93	54.99	51.90	53.71
TiO_2	1.43	1.42	1.46	1.37
Al_2O_3	18.49	18.41	20.11	19.32
Fe_2O_3T	7.39	7.39	7.63	7.24
MnO	0.10	0.10	0.11	0.10
MgO	3.48	3.50	3.77	3.59
CaO	7.41	7.40	8.21	7.80
Na_2O	3.90	3.93	4.45	4.25
K_2O	1.19	1.20	1.24	1.18
P_2O_5	0.20	0.19	0.22	0.22
LOI	1.12	1.03	1.06	1.09
TOTAL	99.64	99.56	100.16	99.87
Li	23.34	24.94	21.21	19.92
Be	1.40	1.40	1.35	0.62
Sc	18.40	18.37	18.05	18.29
V	136.93	138.02	137.09	137.70
Cr	7.48	7.47	8.52	17.20
Co	97.86	93.44	80.79	82.99
Ni	7.23	7.25	6.87	6.99
Cu	12.19	12.22	9.83	11.77
Zn	71.51	71.65	73.56	78.06
Ga	21.08	21.15	20.49	20.62
Ge	1.17	1.19	0.95	0.90
Rb	39.22	39.20	39.33	38.41
Sr	434.14	433.72	415.96	404.93
Y	27.31	27.27	25.59	26.42
Zr	166.73	157.98	165.39	174.26
Nb	5.69	5.72	5.42	5.50
Cs	5.04	5.05	4.87	4.93
Ba	254.51	253.52	246.92	242.87
La	12.93	13.18	14.81	15.05
Ce	31.95	32.65	35.00	36.60
Pr	4.39	4.45	4.20	4.25
Nd	20.06	20.30	20.08	20.40
Sm	4.98	4.96	4.66	4.82
Eu	1.49	1.48	1.41	1.44
Gd	4.95	4.93	4.71	4.89
Tb	0.83	0.83	0.79	0.81
Dy	5.03	4.98	4.83	4.80
Ho	1.00	1.01	0.87	0.94
Er	2.78	2.80	2.54	2.51
Tm	0.40	0.40	0.40	0.37
Yb	2.48	2.48	2.08	2.16
Lu	0.36	0.36	0.32	0.31
Hf	4.08	3.90	3.83	3.97
Ta	0.53	0.52	0.53	0.48
Pb	7.71	7.61	8.23	7.49
Th	1.38	1.39	1.99	1.98
U	0.64	0.63	0.57	0.56

References

1. Şengör, A.M.C.; Natal'in, B.A.; Sunal, G.; van der Voo, R. The Tectonics of the Altaids: Crustal Growth During the Construction of the Continental Lithosphere of Central Asia between ~750 and ~130 Ma Ago. *Annu. Rev. Earth Planet. Sci.* **2018**, *46*, 439–494. [CrossRef]
2. Şengör, A.M.C.; Natal'in, B.A.; Burtman, V.S. Evolution of the Altaid tectonic collage and Palaeozoic crustal growth in Eurasia. *Nature* **1993**, *364*, 299–307. [CrossRef]
3. Xiao, W.; Windley, B.F.; Sun, S.; Li, J.; Huang, B.; Han, C.; Yuan, C.; Sun, M.; Chen, H. A tale of amalgamation of three Permo-Triassic collage systems in Central Asia: Oroclines, sutures, and terminal accretion. *Annu. Rev. Earth Planet. Sci.* **2015**, *43*, 477–507. [CrossRef]

4. Xiao, W.; Windley, B.F.; Han, C.; Liu, W.; Wan, B.; Zhang, J.; Ao, S.; Zhang, Z.; Song, D. Late Paleozoic to early Triassic multiple roll-back and oroclinal bending of the Mongolia collage in Central Asia. *Earth-Sci. Rev.* **2018**, *186*, 94–128. [CrossRef]
5. Windley, B.F.; Alexeiev, D.; Xiao, W.; Kröner, A.; Badarch, G. Tectonic models for accretion of the Central Asian Orogenic Belt. *J. Geol. Soc. Lond.* **2007**, *164*, 31–47. [CrossRef]
6. Zhao, G.; Wang, Y.; Huang, B.; Dong, Y.; Li, S.; Zhang, G.; Yu, S. Geological reconstructions of the East Asian blocks: From the breakup of Rodinia to the assembly of Pangea. *Earth-Sci. Rev.* **2018**, *186*, 262–286. [CrossRef]
7. Xu, B.; Wang, Z.; Zhang, L.; Wang, Z.; Yang, Z.; He, Y. The Xing-Meng intracontinent orogenic belt. *Acta Petrol. Sin.* **2018**, *34*, 2819–2844.
8. Niu, Y.; Liu, C.; Shi, G.R.; Lu, J.; Xu, W.; Shi, J. Unconformity-bounded Upper Paleozoic megasequences in the Beishan Region (NW China) and implications for the timing of the Paleo-Asian Ocean closure. *J. Asian Earth Sci.* **2018**, *167*, 11–32. [CrossRef]
9. Niu, Y.; Shi, G.R.; Ji, W.; Zhou, J.; Wang, J.; Wang, K.; Bai, J.-K.; Yang, B. Paleogeographic evolution of a Carboniferous–Permian sea in the southernmost part of the Central Asian Orogenic Belt, NW China: Evidence from microfacies, provenance and paleobiogeography. *Earth-Sci. Rev.* **2021**, *220*, 103738. [CrossRef]
10. Tang, J.; Zhang, Z.; Xue, J.; Liu, B.; Chen, Y.; Zhang, S. Permo-Carboniferous provenance shifts at the northern margin of the North China Craton and their tectonic implications: Detrital zircon U–Pb–Hf records from central Inner Mongolia. *Gondwana Res.* **2021**, *95*, 134–148. [CrossRef]
11. Zhang, S.; Wang, J.; Liu, C.; Bai, J.; Peng, H.; Huang, H.; Guan, Y. Detrital zircon U–Pb geochronology of the Permian strata in the Turpan–Hami Basin in North Xinjiang, NW China: Depositional age, provenance, and tectonic implications. *Geol. J.* **2019**, *54*, 1064–1080. [CrossRef]
12. Eizenhöfer, P.R.; Zhao, G. Solonker Suture in East Asia and its bearing on the final closure of the eastern segment of the Palaeo-Asian Ocean. *Earth-Sci. Rev.* **2018**, *186*, 153–172. [CrossRef]
13. Han, Y.; Zhao, G. Final amalgamation of the Tianshan and Junggar orogenic collage in the southwestern Central Asian Orogenic Belt: Constraints on the closure of the Paleo-Asian Ocean. *Earth-Sci. Rev.* **2018**, *186*, 129–152. [CrossRef]
14. Bai, J.; Liu, C.; Zhang, S.; LU, J.; Sun, J. Zircon U-Pb geochronology and geochemistry of basalts from the Qi'eshan Group in the southern Turpan-Hami Basin, East Tianshan: Constraints on closure time of the North Tianshan Ocean. *Acta Petrol. Sin.* **2018**, *34*, 2995–3010.
15. Yang, G.; Li, Y.; Tong, L.; Wang, Z.; Si, G. An Early Cambrian Plume-Induced Subduction Initiation Event within the Junggar Ocean: Insights from Ophiolitic Mélanges, Arc Magmatism, and Metamorphic Rocks. *Gondwana Res.* **2020**, *88*, 45–66. [CrossRef]
16. Yang, G.; Li, Y.; Tong, L.; Wang, Z.; Si, G.; Lindagato, P.; Zeng, R. Natural Observations of Subduction Initiation: Implications for the Geodynamic Evolution of the Paleo-Asian Ocean. *Geosyst. Geoenviron.* **2022**, *1*, 100009. [CrossRef]
17. Zhao, X.; Liu, C.; Wang, J.; Zhang, S.; Guan, Y. Geochemistry, geochronology and Hf isotope of granitoids in the northern Alxa region: Implications for the Late Paleozoic tectonic evolution of the Central Asian Orogenic Belt. *Geosci. Front.* **2020**, *11*, 1711–1725. [CrossRef]
18. Song, D.; Xiao, W.; Collins, A.S.; Glorie, S.; Han, C.; Li, Y. Final Subduction processes of the Paleo-Asian Ocean in the Alxa Tectonic Belt (NW China): Constraints from field and chronological data of Permian arc-related volcano-sedimentary rocks. *Tectonics* **2018**, *37*, 1658–1687. [CrossRef]
19. Chen, Y.; Wu, T.; Zhang, Z.; Fanning, C.M.; Zhang, M. Provenance of the Permo–Carboniferous sediments in the northern Alxa and its tectonic implications for the southernmost Central Asian Orogenic Belt. *Geosci. Front.* **2020**, *11*, 1415–1429. [CrossRef]
20. Liu, Q.; Zhao, G.; Han, Y.; Zhu, Y.; Wang, B.; Eizenhöfer, P.R.; Zhang, X.; Tsui, R.W. Timing of the final closure of the middle segment of the Paleo-Asian Ocean: Insights from geochronology and geochemistry of Carboniferous–Triassic volcanosedimentary successions in western Inner Mongolia, China. *GSA Bull.* **2019**, *131*, 941–965. [CrossRef]
21. Tian, R.; Xie, G.; Zhu, W.; Zhang, J.; Gao, S.; Zhang, B.; Zhao, H.; Li, T. Late Paleozoic Tectonic Evolution of the Paleo-Asian Ocean in the Northern Alxa Block (NW China). *Tectonics* **2020**, *39*, e2020TC006359. [CrossRef]
22. Feng, J.; Xiao, W.; Windley, B.; Han, C.; Wan, B.; Zhang, J.; Ao, S.; Zhang, Z.; Lin, L. Field geology, geochronology and geochemistry of mafic–ultramafic rocks from Alxa, China: Implications for Late Permian accretionary tectonics in the southern Altaids. *J. Asian Earth Sci.* **2013**, *78*, 114–142. [CrossRef]
23. Wu, T.; He, G. Tectonic units and their Fundamental characteristics on the northern margin of the Alxa block. *Acta Geol. Sin. Ed.* **1993**, *6*, 373–385. [CrossRef]
24. Zuza, A.V.; Yin, A. Balkatach hypothesis: A new model for the evolution of the Pacific, Tethyan, and Paleo-Asian oceanic domains. *Geosphere* **2017**, *13*, 1664–1712. [CrossRef]
25. Zhang, W.; Wu, T.; Feng, J.; Zheng, R.; He, Y. Time constraints for the closing of the Paleo-Asian Ocean in the Northern Alxa Region: Evidence from Wuliji granites. *Sci. China Earth Sci.* **2013**, *56*, 153–164. [CrossRef]
26. Lu, J.; Shi, J.; Niu, Y.; Song, B.; Zhang, Y.; Yu, L. The Carboniferous-Permian sequence stratigraphy and sedimentary evolution of Beishan-Yin'e region, western Inner Mongolia. *Acta Petrol. Sin.* **2018**, *34*, 3101–3115.
27. Liu, Q.; Zhao, G.; Han, Y.; Eizenhöfer, P.R.; Zhu, Y.; Hou, W.; Zhang, X. Timing of the final closure of the Paleo-Asian Ocean in the Alxa Terrane: Constraints from geochronology and geochemistry of Late Carboniferous to Permian gabbros and diorites. *Lithos* **2017**, *274–275*, 19–30. [CrossRef]
28. Song, D.; Xiao, W.; Windley, B.F.; Mao, Q.; Ao, S.; Wang, H.Y.C.; Li, R. Closure of the Paleo-Asian Ocean in the Middle-Late Triassic (Ladinian-Carnian): Evidence From Provenance Analysis of Retroarc Sediments. *Geophys. Res. Lett.* **2021**, *48*, e2021GL094276. [CrossRef]
29. Cui, X.; Sun, M.; Zhao, G.; Zhang, Y. Origin of Permian mafic intrusions in southern Chinese Altai, Central Asian Orogenic Belt: A post-collisional extension system triggered by slab break-off. *Lithos* **2021**, *390–391*, 106112. [CrossRef]

30. Zhou, W.; Li, H.; Chang, F.; Lv, X. The Early Silurian Gabbro in the Eastern Kunlun Orogenic Belt, Northeast Tibet: Constraints on the Proto-Tethyan Ocean Closure. *Minerals* **2020**, *10*, 794. [CrossRef]

31. Wang, J.; Wang, X.; Liu, J.; Liu, Z.; Zhai, D.; Wang, Y. Geology, geochemistry, and geochronology of gabbro from the Haoyaoer-hudong gold deposit, Northern Margin of the North China Craton. *Minerals* **2019**, *9*, 63. [CrossRef]

32. Zhang, S.; Liu, C.; Bai, J.; Wang, J.; Ming, M.A.; Guan, Y.; Peng, H. Provenance Variability of the Triassic Strata in the Turpan-Hami Basin: Detrital Zircon Record of Indosinian Tectonic Reactivation in the Eastern Tianshan. *Acta Geol. Sin.* **2019**, *93*, 1850–1868. [CrossRef]

33. Zheng, R.; Wu, T.; Zhang, W.; Xu, C.; Meng, Q.; Zhang, Z. Late Paleozoic subduction system in the northern margin of the Alxa block, Altaids: Geochronological and geochemical evidences from ophiolites. *Gondwana Res.* **2014**, *25*, 842–858. [CrossRef]

34. Shi, X.; Wang, T.; Zhang, L.; Castro, A.; Xiao, X.; Tong, Y.; Zhang, J.; Guo, L.; Yang, Q. Timing, petrogenesis and tectonic setting of the Late Paleozoic gabbro–granodiorite–granite intrusions in the Shalazhashan of northern Alxa: Constraints on the southernmost boundary of the Central Asian Orogenic Belt. *Lithos* **2014**, *208*, 158–177. [CrossRef]

35. Zhang, J.; Gong, J. Revisiting the nature and affinity of the Alxa Block. *Acta Petrol. Sin.* **2018**, *34*, 940–962.

36. Tian, R.; Xie, G.; Zhu, W.; Gao, S. Late Paleozoic magmatic flare-up in the Nuoergong-Langshan Belt, Alxa Block: Insights into tectonic evolution of the southern Paleo-Asian Ocean. *Lithos* **2021**, *398–399*, 106310. [CrossRef]

37. Ludwig, K. *User's Manual for Isoplot Version 3.75–4.15: A Geochronological Toolkit for Microsoft*; Berkeley Geochronology Center: Berkeley, CA, USA, 2012.

38. Liu, Y.; Liu, X.; Hu, Z.; Diwu, C.; Yuan, H.; Gao, S. Evaluation of accuracy and long-term stability of determination of 37 trace elements in geological samples by ICP-MS. *Acta Petrol. Sin.* **2007**, *23*, 1203–1210.

39. Yuan, H.-L.; Gao, S.; Dai, M.-N.; Zong, C.-L.; Günther, D.; Fontaine, G.H.; Liu, X.-M.; Diwu, C. Simultaneous determinations of U–Pb age, Hf isotopes and trace element compositions of zircon by excimer laser-ablation quadrupole and multiple-collector ICP-MS. *Chem. Geol.* **2008**, *247*, 100–118. [CrossRef]

40. Sang, H.; Wang, F.; He, H.; Wang, Y.; Yang, L.; Zhu, R. Intercalibration of ZBH-25 Biotite Reference Material Untilized for K-Ar and Ar-40-Ar-39 Age Determination. *Acta Petrol. Sin.* **2006**, *22*, 3059–3078.

41. Zhou, B.; Dong, Y.; Yang, Z.; Genser, J.; Liu, X. Laser Fusion ^{40}Ar-^{39}Ar Dating Method Using Multi-Collector Noble Gas Mass Spectrometer Argus VI and Its Geological Application. *Earth Sci. China Univ. Geosci.* **2020**, *45*, 804. [CrossRef]

42. Koppers, A.A. ArArCALC—Software for ^{40}Ar/^{39}Ar age calculations. *Comput. Geosci.* **2002**, *28*, 605–619. [CrossRef]

43. Steiger, R.H.; Jäger, E. Subcommission on geochronology: Convention on the use of decay constants in geo- and cosmochronology. *Earth Planet. Sci. Lett.* **1977**, *36*, 359–362. [CrossRef]

44. Cox, K.G.; Bell, J.D.; Pankhurst, R.J. *The Interpretation of Igneous Rocks*; Chapman & Hall: London, UK, 1979.

45. Middlemost, E.A.K. *Magmas and Magmatic Rocks: An Introduction to Igneous Petrology*; Addison-Wesley Longman: Boston, MA, USA, 1985.

46. Wright, J.B. A simple alkalinity ratio and its application to questions of non-orogenic granite genesis. *Geol. Mag.* **1969**, *106*, 370–384. [CrossRef]

47. Maniar, P.D.; Piccoli, P.M. Tectonic discrimination of granitoids. *Geol. Soc. Am. Bull.* **1989**, *101*, 635–643. [CrossRef]

48. Taylor, S.R.; McLennan, S.M. *The Continental Crust: Its Composition and Evolution*; Blackwell Scientific Publications: Hoboken, NJ, USA, 1985; p. 312. ISBN 0632011483.

49. Sun, S.S.; McDonough, W.F. Chemical and isotopic systematics of oceanic basalts: Implications for mantle composition and processes. *Geol. Soc. Spec. Publ.* **1989**, *42*, 313–345. [CrossRef]

50. Liu, Z.; Zhang, X.; Tan, S.-C.; Sha, X.; He, X.-H.; Zhou, Q. The Timing of the Paleo-Asian Oceanic Closure: Geochemical Constraints from the Jigede Gabbro in the Alxa Block. *Petrology* **2019**, *27*, 425–437. [CrossRef]

51. Tikoff, B.; Blenkinsop, T.; Kruckenberg, S.C.; Morgan, S.; Newman, J.; Wojtal, S. A perspective on the emergence of modern structural geology: Celebrating the feedbacks between historical-based and process-based approaches. In *The Web of Geological Sciences: Advances, Impacts, and Interactions: Geological Society of America Special Paper 500*; Geological Society of America: Boulder, CO, USA, 2013; pp. 65–119.

52. Iizuka, T.; Yamaguchi, T.; Itano, K.; Hibiya, Y.; Suzuki, K. What Hf isotopes in zircon tell us about crust–mantle evolution. *Lithos* **2017**, *274–275*, 304–327. [CrossRef]

53. Wu, F.Y.; Li, X.H.; Zheng, Y.F.; Gao, S. Lu-Hf isotopic systematics and thier applications in petrology. *Acta Petrol. Sin.* **2007**, *23*, 185–220.

54. Taylor, S.R.; McLennan, S.M. The geochemical evolution of the continental crust. *Rev. Geophys.* **1995**, *33*, 241–265. [CrossRef]

55. Yu, Y.; Huang, X.L.; Sun, M.; Yuan, C. Missing Sr–Nd isotopic decoupling in subduction zone: Decoding the multi-stage dehydration and melting of subducted slab in the Chinese Altai. *Lithos* **2020**, *362–363*, 105465. [CrossRef]

56. Zafar, T.; Leng, C.B.; Mahar, M.A.; Alam, M.; Zhang, X.C.; Chen, W.T.; Rehman, H.U.; Rehman, S.U. Petrogenesis, platinum-group element geochemistry and geodynamic evolution of the Cretaceous Chilas gabbros, Kohistan island arc, NE Pakistan. *Lithos* **2020**, *372–373*, 105691. [CrossRef]

57. Frey, F.A.; Green, D.H.; Roy, S.D. Integrated models of basalt petrogenesis: A study of quartz tholeiites to olivine melilitites from South Eastern Australia utilizing geochemical and experimental petrological data. *J. Petrol.* **1978**, *19*, 463–513. [CrossRef]

58. Saunders, A.D.; Storey, M.; Kent, R.W.; Norry, M.J. Consequences of plume-lithosphere interactions. *Geol. Soc. Lond. Spec. Publ.* **1992**, *68*, 41–60. [CrossRef]

59. Pearce, J.A. Geochemical fingerprinting of oceanic basalts with applications to ophiolite classification and the search for Archean oceanic crust. *Lithos* **2008**, *100*, 14–48. [CrossRef]

60. Kepezhinskas, P.; McDermott, F.; Defant, M.J.; Hochstaedter, A.; Drummond, M.S.; Hawkesworth, C.J.; Koloskov, A.; Maury, R.C.; Bellon, H. Trace element and Sr-Nd-Pb isotopic constraints on a three-component model of Kamchatka Arc petrogenesis. *Geochim. Cosmochim. Acta* **1997**, *61*, 577–600. [CrossRef]

61. Martin, H.; Smithies, R.H.; Rapp, R.; Moyen, J.-F.; Champion, D. An overview of adakite, tonalite–trondhjemite–granodiorite (TTG), and sanukitoid: Relationships and some implications for crustal evolution. *Lithos* **2005**, *79*, 1–24. [CrossRef]

62. Pearce, J.A.; Norry, M.J. Petrogenetic implications of Ti, Zr, Y, and Nb variations in volcanic rocks. *Contrib. Mineral. Petrol.* **1979**, *69*, 33–47. [CrossRef]

63. Meschede, M. A method of discriminating between different types of mid-ocean ridge basalts and continental tholeiites with the Nb-Zr-Y diagram. *Chem. Geol.* **1986**, *56*, 207–218. [CrossRef]

64. Song, D.; Glorie, S.; Xiao, W.; Collins, A.S.; Gillespie, J.; Jepson, G.; Li, Y. Tectono-thermal evolution of the southwestern Alxa Tectonic Belt, NW China: Constrained by apatite U-Pb and fission track thermochronology. *Tectonophysics* **2018**, *722*, 577–594. [CrossRef]

65. Zhang, J.; Wang, Y.; Qu, J.; Zhang, B.; Zhao, H.; Yun, L.; Li, T.; Niu, P.; Nie, F.; Hui, J.; et al. Mesozoic intracontinental deformation of the Alxa Block in the middle part of Central Asian Orogenic Belt: A review. *Int. Geol. Rev.* **2021**, *63*, 1490–1520. [CrossRef]

66. Liu, S.; Qian, T.; Li, W.; Dou, G.; Wu, P. Oblique closure of the northeastern Paleo-Tethys in central China. *Tectonics* **2015**, *34*, 413–434. [CrossRef]

67. Zhang, S.; Liu, C.; Yang, M.; Bai, J.; Wang, J. Latest Triassic to Early Jurassic Thrusting and Exhumation in the Southern Ordos Basin, North China: Evidence from LA-ICP-MS-based Apatite Fission Track Thermochronology. *Acta Geol. Sin. Ed.* **2018**, *92*, 1334–1348. [CrossRef]

68. Pullen, A.; Kapp, P.; Gehrels, G.E.; Vervoort, J.D.; Ding, L. Triassic continental subduction in central tibet and Mediterranean-style closure of the Paleo-Tethys Ocean. *Geology* **2008**, *36*, 351–354. [CrossRef]

69. Zhao, P.; Appel, E.; Xu, B. An Inclination Shallowing-Corrected Early Triassic Paleomagnetic Pole for the North China Craton: Implication for the Mesozoic Geography of Proto-Asia. *J. Geophys. Res. Solid Earth* **2020**, *125*, e2020JB019489. [CrossRef]

70. Zhang, S.; Liu, C.; Yang, M.; Wang, J.; Bai, J.; Huang, H. Decoding Provenance and Tectonothermal Events by Detrital Zircon Fission-Track and U-Pb Double Dating: A Case of the Southern Ordos Basin. *Acta Geol. Sin.* **2019**, *93*, 845–856. [CrossRef]